Jour. Korean Earth Science Society, Vol. 23, No. 1, p. 59–71, January 2002

Radiative Transfer Simulation of Microwave Brightness Temperature from Rain Rate

Jung-Moon Yoo*

Department of Science Education, EWHA Womans University

Abstract: Theoretical models of radiative transfer are developed to simulate the 85 GHz brightness temperature (T85) observed by the Tropical Rainfall Measuring Mission (TRMM) Microwave Imager (TMI) radiometer as a function of rain rate. These simulations are performed separately over regions of the convective and stratiform rain. TRMM Precipitation Radar (PR) observations are utilized to construct vertical profiles of hydrometeors in the regions. For a given rain rate, the extinction in 85 GHz due to hydrometeors above the freezing level is found to be relatively weak in the convective regions compared to that in the stratiform. The hydrometeor profile above the freezing level responsible for the weak extinction in convective regions is inferred from theoretical considerations to contain two layers: 1) a mixed (or mixed-phase) layer of 2 km thickness with mixed-phase particles, liquid drops and graupel above the freezing level, and 2) a layer of graupel extending from the top of the mixed layer to the cloud top. Strong extinction in the stratiform regions is inferred to result from slowly-falling, low-density ice aggregates (snow) above the freezing level. These theoretical results are consistent with the T85 measured by TMI, and with the rain rate deduced from PR for the convective and stratiform rain regions. On the basis of this study, the accuracy of the rain rate sensed by TMI is inferred to depend critically on the specification of the convective or stratiform nature of the rain.

Key words: radiative transfer, TRMM, TMI, convective, stratiform, rain rate, brightness temperature, precipitation radar, mixed layer

INTRODUCTION

In atmospheric columns with convective rain, the nature of hydrometeors has been observed to differ significantly from that in columns with stratiform rain (e.g., see Houze, 1993, 1997). This is mainly because of differences in the dynamics associated with two rain types. In convective regions, low-level convergence of moist air results in updrafts that can have speeds of several ms^{-1}. Furthermore, in convection rain drops grow by the collision-coalescence mechanism below the freezing level. Above the freezing level, the relatively strong vertical motions lead to a mixed (or mixed-phase) layer of coexisting water and ice particles that can extend to altitudes where temperatures are $-10°C$ or lower (see Smith *et al.*, 1999; Bringi *et al.*, 1997; Balakrishnan and Zrnic, 1990; Sax and Keller, 1980). Radar reflectivity factor (Z) measurements in the convective region indicate an appreciable variability in the horizontal direction. The typical scale of the convective cells is on the order of a few kilometers. However, these cells often exist together on a scale of about 20 km, which corresponds to the scale of thunderstorms (Cb). Thus, to get fine information about convective rain, an observing instrument should have a field of view of about 2 km. On the other hand, as the resolution degrades, details of the Cb can still be perceived approximately.

In contrast to the dynamics associated with convective rain, in the stratiform rain region there is weak mesoscale convergence near cloud base, which leads to weak rising motion above. Z measurements show that in the stratiform rain region there is a relatively uniform distribution of hydrometeors horizontally. The growth of hydrometeors takes place mainly above the freezing level, and is due to deposition of water vapor on slowly-falling ice particles that form large, low-density ice aggregates (snow) (see Sekhon and Srivastava, 1970). In stratiform

*E-mail: yjm@mm.ewha.ac.kr

rain regions, the mixed layer above the freezing level is not prominent due to weak vertical motions (~0.5 ms^{-1}). Below the freezing level, snow usually melts before it can fall a distance of 500 m. Under favorable conditions, this melting layer is distinguished by a peak in the radar reflectivity factor profile, or bright band. Beneath this melting layer, rain drops essentially originate from the relatively-large, fully-melted snowflakes. For a given rain rate, the mode diameter of drop size present in stratiform rain is found to be larger than that in convective rain (see Short *et al.*, 1997). In the estimation of near-surface rain rate (R) based on radar reflectivity factor, this difference in drop size distribution between convective and stratiform rain is incorporated in the form of separate Z-R relationships. Thus, it follows that the presence of a bright band in the vertical profile and horizontal variability of Z is needed in the inference of rain type and estimation of rain rate from radar data (Iguchi *et al.*, 2000).

In order to examine the connection between radar and passive microwave radiometer observations, the nearly simultaneous measurements of the Tropical Rainfall Measuring Mission (TRMM) Microwave Imager (TMI) radiometer and Precipitation Radar (PR) onboard the TRMM satellite have been analyzed in this study. In particular, the vertical Z profiles given by the PR have been compared with T85 measured by the TMI. This is done separately for the convective and stratiform rain areas. The purpose of this study is to develop radiative transfer models that simulate T85 as a function of rain rate in the convective and stratiform rain regions, based on observations of TMI and PR.

RELATIONSHIP BETWEEN TMI AND PR OBSERVATIONS IN THE CONVECTIVE AND STRATIFORM RAIN REGIONS

The near-surface rain information deduced from PR data has a horizontal resolution of about 4.3 km×4.3 km. The data are arranged uniformly at a spacing of 4.3 km both along and across scan lines. On the other hand, the 85 GHz footprints of TMI are approximately 5.0 km×7.0 km, and are separated by about 5.0 km along scan lines and about 14 km across scan lines. This scan pattern degrades the effective resolution of the TMI 85 GHz channel, compared with the PR resolution. The TMI additionally contains the channels in vertical and horizontal polarization at 10.7, 19, and 37 GHz that have a resolution of about 40, 20, and 10 km, respectively. Furthermore, TMI has a 21 GHz channel in vertical polarization that has a resolution similar to that of 19 GHz. Since the resolution of the 85 GHz channel is closest to that of the PR, the information given by this channel and the PR is analyzed together in this study.

In addition to differences in resolution, spatial mismatch between the data of the TMI and PR causes problems in coordinating the information given by these two instruments. Such spatial mismatch arises primarily for two reasons. First, the TMI has a conical viewing geometry, while the PR has a cross-track viewing geometry. Secondly, the rain information given by the PR corresponds to lower atmospheric layers, while the 85 GHz temperature responds strongly to the ice hydrometeors in the upper layers above the freezing level (Wu and Weinman, 1984). Thus, vertical difference of hydrometeors between the upper and lower levels can create spatial mismatch in the TMI and PR observations. For these two reasons, in order to compare the PR and TMI observations, it is assumed that averaging the data of each instrument to the Cb scale (~20 km) will minimize the effects of spatial mismatch. However, since the hydrometeors originated at higher altitudes take several minutes to reach the near-surface layers, the assumption is not exact. This is because it presupposes that the hydrometeors above and below the freezing level in rain systems are in a relative steady state.

Based on the above assumptions, the mean brightness temperatures given by TMI have been calculated over 20 km pixels. For the same pixels, the

Table 1. The date, time, and location for 20 MCS events over land observed by the TRMM satellite. Also given are the number of convective and stratiform pixels for each rain event.

Number	Month	Day	Time	Lat	Long	Region	No of conv pixels	No of strat pixels
1	'98 Jan	9	528	−4.65	−74.20	Amazon	3	94
2	'99 Jan	19	1820	−17.90	29.75	Africa	1	24
3	'99 Feb	13	1431	−17.20	127.50	Australia	12	13
4	'98 Jun	5	708	32.75	−92.00	USA	10	1
5	'98 Jun	5	845	35.00	−89.10	USA	27	40
6	'98 Jun	8	2010	12.50	−1.40	Africa	5	11
7	'98 Jun	9	1030	4.40	−66.20	Amazon	0	62
8	'98 Jun	11	441	33.00	−99.50	USA	13	14
9	'98 Jun	18	1500	26.90	115.70	China	3	66
10	'98 Jun	20	1411	25.80	115.00	China	4	17
11	'98 Jun	29	456	32.75	116.00	China	12	19
12	'98 Jul	1	829	12.20	−2.20	Africa	12	27
13	'98 Jul	5	223	24.00	81.50	India	7	29
14	'98 Jul	20	1648	28.90	116.00	China	2	18
15	'98 Jul	20	2247	17.80	−0.05	Africa	20	27
16	'99 Jul	11	157	25.00	84.10	India	14	54
17	'99 Jul	22	405	4.60	−69.30	Amazon	11	17
18	'99 Jul	29	2018	14.45	2.50	Africa	13	15
19	'99 Sep	16	413	34.20	−78.20	USA	11	62
20	'98 Dec	28	1034	−26.70	−58.00	South America	30	40

mean near-surface rain rate and profile of reflectivity factor given by the PR have been also calculated. For the purpose of this study, a given PR observation is assumed to have zero near-surface rain rate when R deduced from PR is less than 0.1 $mmhr^{-1}$. The PR data show that the rain rate can be highly variable in space in a given 20 km pixel. There are about 17 PR footprints of 4.3 km×4.3 km in a given pixel. The 17 footprints can be sorted with the PR classification as having no rain, stratiform rain, or convective rain. In this study, a 20 km pixel is categorized as convective when 50% or more of its area is covered by convective rain type. Similarly, a pixel is categorized as stratiform when 80% or more of its area is covered by stratiform rain type. Each of these convective and stratiform rain pixels is generally found to have a rain-free area that is small (< 25%). However, the pixels constitute only about 15% of the total number of pixels in a given Mesoscale Convective System (MCS). The remaining 85% of pixels are neither dominantly convective nor stratiform, and could have substantial areas with no rain.

For the purpose of generating a set of TMI and PR data associated with the convective and stratiform pixels, 20 MCS rain events observed by the TRMM satellite over diverse land regions of the tropics have been utilized. The time, location, and the number of convective and stratiform pixels for each MCS case are presented in Table 1. The pixels have been mostly obtained during the summer of each hemisphere when convective activity is high.

In Fig. 1, a plot of T85 and the corresponding PR rain rate averaged over 20 km pixels is presented. The values of T85 and PR rain rate have been taken from the 20 MCS events listed in Table 1. Here the pixels characterized as convective by the PR have relatively high rain rates, while the pixels characterized as stratiform have generally low rain rates. A closer examination of the PR data shows that more than 90% of the convective pixels have rain rates greater than 10 $mmhr^{-1}$, even at warm brightness temperatures as high as 260 K. Also, more than 97% of the stratiform pixels have rain rates less than 10 $mmhr^{-1}$. Although there is no reason to expect a linear relationship between T85 given by the TMI and R given by PR, for a simple comparison, the slope dR/dT85 given by linear regression for convective rain is three to four times larger than that for stratiform (Fig. 1). In this

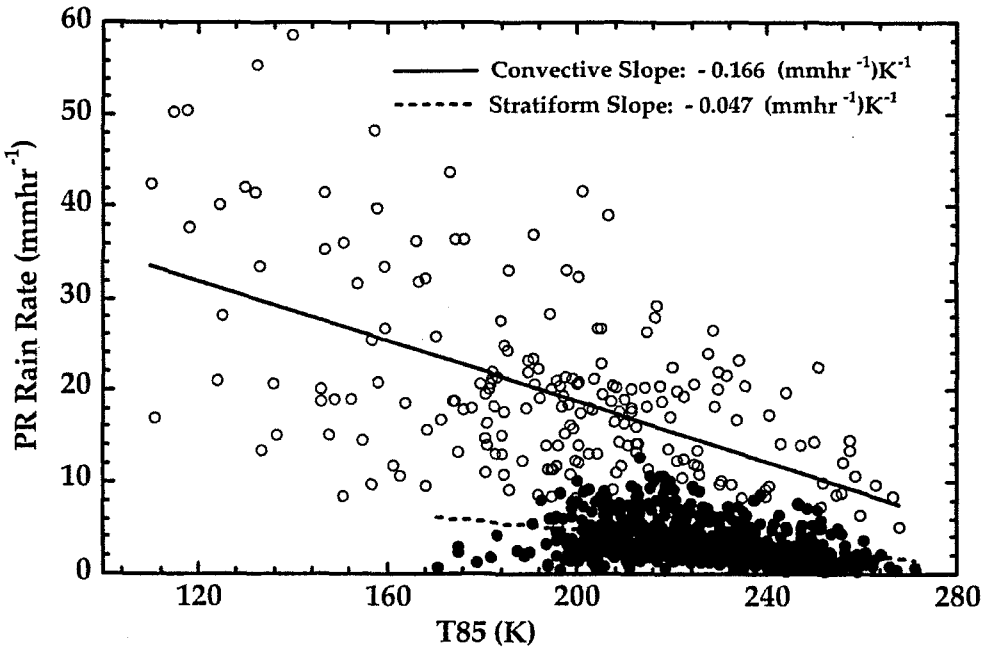

Fig. 1. Observed PR rain rate versus T85 for 20 km pixels. The open circles denote convective pixels, while the filled circles represent stratiform pixels. The linear regression line fitting PR rain rate to T85 for the convective pixels is given by the solid line, while for the stratiform pixels it is shown by the dashed line. The slope of these regression lines is also provided in the plot. Data for this plot are taken from TRMM observations of 20 MCS cases over land.

study, the difference in the slopes between convective and stratiform rain types will be discussed later with the help of radiative transfer models (Fig. 6).

To enhance statistical strength in the pixel data described above, additional averaging has been performed over the TMI brightness temperatures, and over the near-surface rain rates given by PR, in 20 K intervals of T85 (Tables 2-3). The averaging has also been done for the PR reflectivity factor at various altitudes to obtain mean profiles of reflectivity factor. The averaging for the 10.7 GHz and 21 GHz channels has not been done. The TMI 10.7 GHz channel has a field of view much larger than 20 km, while the information given by the 21 GHz does not differ significantly from that by the 19 GHz channel.

Table 2. Average of PR and TMI 20 km pixel observations within a given 20 K interval of T85 for convective rain. The averages are calculated for the following parameters: T85, T37, T19, convective rain fraction, PR near-surface rain rate (R), and PR reflectivity facor (Z) at 1, 3, 4, 4.5, 6, 7, 9, and 11 km. The number of 20 km pixel observations in a given T85 interval is also shown in the table. The population of pixels used to generate these statistics associated with convective rain is deduced from 20 MCS cases over land regions. Overbar in the table stands for average value.

T85 interval (K)	No of pixels	$\overline{T85}$ (K)	$\overline{T37}$ (K)	$\overline{T19}$ (K)	Conv rain frac (%)	$\overline{R}$ (mm/hr)	Average Z							
							1 km	3 km	4 km	4.5 km	6 km	7 km	9 km	11 km
110 ~ 130	9	119.3	202.0	257.7	73	36.7	9.4E4	1.2E5	9.2E4	7.0E4	2.0E4	9.0E3	2.6E3	1.0E3
130 ~ 150	13	140.3	210.7	257.4	70	29.9	8.8E4	1.1E5	7.6E4	5.4E4	1.7E4	9.4E3	2.4E3	7.6E2
150 ~ 170	20	159.5	224.7	262.3	66	24.1	5.7E4	5.8E4	4.0E4	2.8E4	8.5E3	4.0E3	1.1E3	3.9E2
170 ~ 190	37	181.0	241.7	267.6	65	20.4	4.5E4	3.6E4	2.6E4	1.9E4	5.7E3	2.8E3	6.3E2	2.6E2
190 ~ 210	58	199.8	251.1	271.3	62	18.6	3.0E4	2.2E4	1.6E4	1.2E4	2.8E3	1.3E3	3.9E2	1.3E2
210 ~ 230	41	219.0	256.4	270.6	61	16.3	2.5E4	1.6E4	1.2E4	9.2E3	2.0E3	7.3E2	1.7E2	8.9E1
230 ~ 250	18	237.7	262.8	274.1	57	13.2	2.2E4	1.4E4	1.2E4	1.1E4	3.4E3	1.2E3	2.9E2	1.3E2
250 ~ 270	14	257.2	269.7	275.7	56	10.3	1.2E4	7.8E3	6.1E3	5.1E3	1.4E3	4.9E2	2.4E2	1.1E1

Table 3. Average of PR and TMI 20 km pixel observations within a given 20 K interval of T85 for stratiform rain. The averages are calculated for the following parameters: T85, T37, T19, stratiform rain fraction; PR near-surface rain rate (R), and PR reflectivity factor (Z) at 1, 3, 4, 4.5, 6, 7, 9, and 11 km. The number of 20 km pixel observations in a given T85 interval is also shown in the table. The population of pixels used to generate these statistics associated with stratiform rain is deduced from 20 MCS cases over land regions. Overbar in the table stand for average value.

T85 interval (K)	No of pixels	$\overline{T85}$ (K)	$\overline{T37}$ (K)	$\overline{T19}$ (K)	Strat rain frac (%)	$\overline{R}$ (mm/hr)	Average Z							
							1 km	3 km	4 km	4.5 km	6 km	7 km	9 km	11 km
170 ~ 190	10	181.8	245.6	268.8	81	2.3	1.4E3	2.0E3	2.0E3	8.6E2	2.3E2	1.8E2	1.0E2	6.8E1
190 ~ 210	132	202.9	254.8	268.4	82	3.7	3.6E3	4.2E3	5.5E3	2.2E3	2.6E2	1.7E2	7.7E1	2.2E1
210 ~ 230	213	219.3	257.5	270.9	83	4.5	3.6E3	3.8E3	6.0E3	3.6E3	2.5E2	1.4E2	5.8E1	1.4E1
230 ~ 250	220	240.0	263.0	273.5	83	2.7	1.7E3	1.3E3	2.8E3	2.2E3	1.2E2	7.7E1	2.3E1	2.5E0
250 ~ 270	74	255.8	265.3	270.3	82	1.8	9.6E2	7.7E2	1.1E3	1.1E3	8.6E1	5.3E1	1.1E1	0.5E0

The pixel-average data for convective rain regions of the 20 MCSs is presented in Table 2. A similar set of data for the stratiform rain regions obtained from the MCS events is presented in Table 3. In Tables 2-3, the number of observations in each T85 interval have also been included. It may be pointed out that the standard deviation of the reflectivity Z at each level for a given T85 interval of 20 K has a magnitude comparable to the mean value itself. Note that an overbar in the tables will be used to represent the mean of T85, T37, T19, and R at each level for each 20 K interval of T85.

In Figs. 2a and 2b, plots of Z at different levels in the atmosphere as a function of T85 are presented using the data given in Tables 2-3. From the figures, as T85 decreases, Z increases. Above the freezing level (4.5 km), there is generally an exponential decrease of mean reflectivity factor with height. The scale height of the exponential decrease is about 1.25 km for convective regions, and about 1.0 km for stratiform. The above observations demonstrate that there is a relationship between T85 and vertical profiles of Z. This information can be used to model the vertical profiles of the hydrometeor content in the convective and stratiform regions. The brightness temperatures in 19 and 37 GHz (T19 and T37) given in Tables 2-3 reveal that they are correlated with the radar reflectivity factor in an analogous way. However, the 19 and 37 GHz channels are less sensitive than the 85 GHz channel.

Based on the data shown in Tables 2-3, T19 and T37 are found to strongly correlate with T85 in

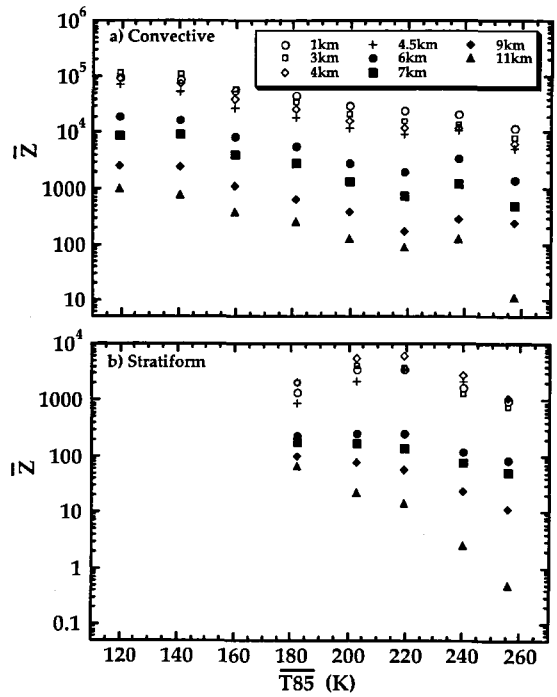

Fig. 2. Log of PR reflectivity, Z, at different levels versus $\overline{T85}$ for a) convective and b) stratiform rain. The levels are given in the panel of upper figure. Overbar in the figure stands for average value.

convective and stratiform regions, as shown in Figs. 3a-b respectively. The strong correlation indicates that the information contained in these radiometer channels is highly redundant. Also for a given set of T19, T37 and T85, one can get widely different rain rates depending on the rain type that is being observed (Tables 2-3). This implies that radiometer data are on the average insensitive to the rain type. On the other hand, Z is found to be quite sen-

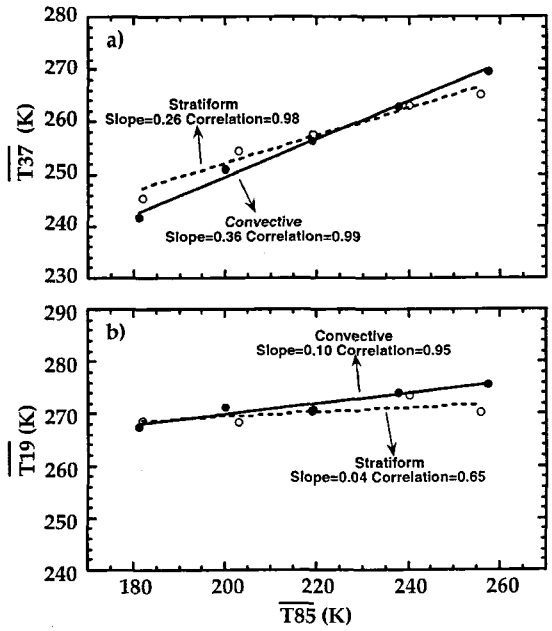

Fig. 3. Scatter plots of a) $\overline{T37}$ versus $\overline{T85}$ and b) $\overline{T19}$ versus $\overline{T85}$ for convective (filled circles) and stratiform (open circles) rain. The linear regression lines in the plots are also given for convective (*solid lines*) and stratiform (*dashed* lines) cases. Furthermore, information regarding the slope and correlation of each regression line is provided. Overbar in the figure stands for average value.

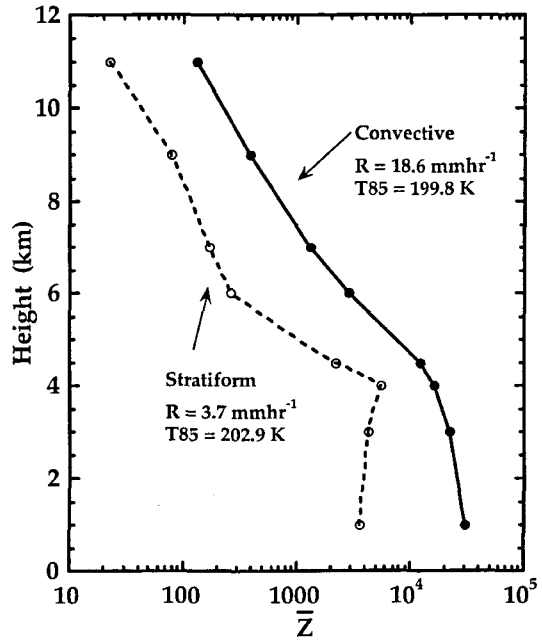

Fig. 4. Convective (solid line) and stratiform (dashed line) vertical profiles of PR reflectivity, Z, for the T85 interval of 190 K to 210 K. In the plot, PR rain rate and T85 are given. Overbar in the figure stand for average value.

sitive to the rain type and to the rain rate from the tables. The reason for this is that PR reflectivity factor depends on the sixth power of the mode drop diameter of rain in a given 250 m thick element of the radar beam. The strong sensitivity to the rain drops is not present in the passive microwave radiometer data, which depends on the third power of drop diameter.

In order to infer the extinction due to hydrometeors in convective and stratiform regions, the following comparison is presented over two profiles of PR reflectivity factor. From Table 2, which gives the average values of the data for convective rain, the Z profile has been taken when T85 is in the interval between 190 K and 210 K. Likewise, the Z for stratiform rain has been taken from Table 3 for the same T85 interval. The mean near-surface rain rate deduced from PR for the convective profile is 18.6 $mmhr^{-1}$, while it is 3.7 $mmhr^{-1}$ for the stratiform. In Fig. 4, these two profiles are compared. Here, although Z at all levels given by the stratiform hydrometeors is generally less than that by the convective, the values of T85 associated with these profiles are not much different. The scattering of radiation due to ice hydrometeors above the freezing level essentially determines the magnitude of T85 (Wu and Weinman, 1984). Thus, it is concluded that even when the rain rate is relatively weak in the stratiform regions, the vertically-integrated mass of ice hydrometeors and their extinction can be substantial. This information is used in the radiative transfer modeling performed in this study.

RADIATIVE TRANSFER EQUATIONS

The radiative transfer equation, including absorption and scattering processes in the atmosphere, and assuming local thermodynamic equilibrium and plane parallel stratification, can be written as follows at a

given frequency of radiation in the microwave region (Chandrasekhar, 1960):

$$-\mu\frac{dT_b(\tau,\mu)}{d\tau} = -T_b(\tau,\mu) + \frac{\omega(\tau)}{2} \int_{-1}^{+1} \mathbf{P}(\mu,\mu')T_b(\tau,\mu')d\mu' + \{1-\omega(\tau)\}T(\tau) \quad (1)$$

The parameters in this equation are:

- $T_b(\tau, \mu)$ - the brightness temperature of radiation along a direction given by the direction cosine μ at an optical depth τ in the atmosphere.
- ω - the single scattering albedo of both the cloud particles and the atmosphere. This can be written as $\omega(\tau) = k_s/(k_s + k_a + k_g) = k_s/k_e$, where k_s, k_a, and k_e are the volume scattering, absorption, and extinction coefficients of the particles. Furthermore, k_g represents the total volume absorption coefficient due to gases in the atmosphere.
- $\mathbf{P}(\mu, \mu')$ - the azimuthally averaged scattering phase function.
- $T(\tau)$ - the local temperature of the atmosphere.

The two boundary conditions to solve Eq. (1) are the brightness temperature downwelling on the top of the atmosphere, and upwelling at the bottom of the atmosphere. These are given below:

$$T_b(\tau = 0, \mu^-) = 3K \quad (2)$$

$$T_b(\tau = \tau_s, \mu^+) = T_s\varepsilon_s(\mu) + \{1 - \varepsilon_s(\mu)\}T_b(\tau = \tau_s, \mu^-) \quad (3)$$

where $T_b(\tau = \tau_s, \mu^-)$ is the downwelling brightness temperature incident on the surface. The parameters T_s and $\varepsilon_s(\mu)$ are the surface temperature and emissivity, respectively.

In this study, this atmosphere is numerically represented with 90 layers between the surface and an altitude of 18 km. Eq. (1) is solved numerically by the method of successive orders of scattering. This method involves computation of the source function and intensity using the recursion relationship between them (e.g. Liou, 1980) for each successive order of scattering. In this study, the method is iterated until the brightness temperature emerging at the top of the atmosphere converges to within 0.1 K.

The Mie computational procedure of Wiscombe (1980) has been used to calculate the volume absorption and scattering coefficients, k_a and k_s, as well as the phase function, **P**. It may be noted that these properties k_a, k_s and **P** depend on the real and imaginary parts of the refractive index (Ray, 1972).

When a given volume of the atmosphere contains both water drops and ice particles, k_s, k_e and $\mathbf{P}(\mu, \mu')$ are defined by

$$k_s = f_{wat}\, k_{swat} + f_{ice}\, k_{sice} \quad (4)$$

$$k_e = f_{wat}\, k_{ewat} + f_{ice}\, k_{eice} \quad (5)$$

$$\mathbf{P}(\mu, \mu') = f_{wat}\, P_{wat}(\mu, \mu') + f_{ice}\, P_{ice}(\mu, \mu') \quad (6)$$

where f_{wat} and f_{ice} are the volume fractions of water drops and ice, respectively, at each level in the mixed layer. Also, in the above equations k_{swat}, k_{ewat}, and $P_{wat}(\mu, \mu')$ are the scattering and extinction coefficients and the phase function for water. Similarly, k_{sice}, k_{eice}, and $P_{ice}(\mu, \mu')$ are the scattering and extinction coefficients and the phase function for ice.

RADIATIVE TRANSFER SIMULATIONS APPLICABLE TO CONVECTIVE/ STRATIFORM REGIONS

Since there is a significant amount of redundancy between the 19, 37, and 85 GHz data, and the 85 GHz channel has the best resolution and the highest sensitivity to hydrometeors associated with precipitation, the 85 GHz brightness temperatures have been simulated. Here separate radiative transfer models are utilized, applicable to the convective and stratiform rain regions, respectively. The characteristics of these different rain types have been described briefly in the introduction. In Figs. 5a-b, typical vertical profiles of the radar reflectivity factor are presented corresponding to the convective and stratiform rain regions, respectively.

For the purpose of these simulations, a tropical

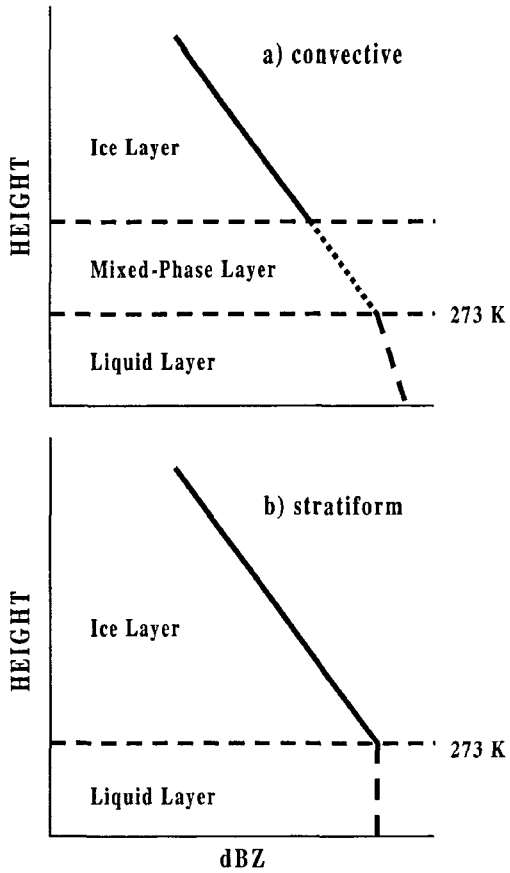

Fig. 5. Microphysical and dBZ profiles used in the radiative transfer model to explain the different rain rate versus T85 relationships of a) convective and b) stratiform rain.

atmosphere has been assumed with a surface temperature of 297 K. The atmosphere has a water vapor distribution that the relative humidity is 80% between the surface and cloud base, and 100% above the base. The temperature lapse rate is 5.5 Kkm^{-1}, which gives a freezing level close to 4.5 km.

For the convective rain regions, the cloud base is set at 1.5 km, and the cloud liquid water content is assumed to increase linearly from 0.5 gm^{-3} to 1.0 gm^{-3} as surface rain rate increases from 2.0 $mmhr^{-1}$ to 32.0 $mmhr^{-1}$. Above the freezing level, cloud water is assumed to decrease exponentially with a scale height of 1.25 km. The nature of the hydrometeors above the freezing level has been studied using reflectivity factor made by radar measurements (Smith *et al.*, 1999; Bringi *et al.*, 1997; Balakrishnan and Zrnic, 1990; Sax and Keller, 1980). The measurements indicate the presence of mixed-phase water and ice particles to a depth of 1 km to 2 km above the freezing level, because of strong vertical motions in convective updrafts (Fig. 5a). Based on the radar studies, in theoretical simulations of this study, the presence of mixed-phase particles is assumed to be in a 2 km layer above the freezing level. In the convective mixed-phase layer containing water drops and graupel, graupel is treated as a mixture of air and ice with a density of 0.4 gcm^{-3}. Above the mixed layer, all hydrometeors are assumed to be frozen graupel with a density of 0.4 gcm^{-1}. The fall speed of graupel as a function of altitude is given using the results of Zikmundu and Vali (1972) and Foote and Du Toit (1969). According to the studies, the average fall speed for graupel with diameters of 1 ~ 5 mm is about 3 ~ 4 ms^{-1}. To resemble the profile of radar reflectivity factor, the total mass m(z) of water drops and graupel per unit volume is assumed to exponentially decrease as a function of height (z) above the freezing level. The corresponding mass per unit volume of graupel and water drops is denoted by $m_g(z)$ and $m_w(z)$, respectively. The vertical profiles of the hydrometeors can be expressed as

$$m_g(z) = m_{ow} C\alpha(z) \exp\left(-\frac{z}{H}\right) \tag{7}$$

$$m_w(z) = m_{ow}\{1-\alpha(z)\} \exp\left(-\frac{z}{H}\right) \tag{8}$$

In Eqs. (7)-(8), m_{ow} stands for the mass per unit volume of water drops and graupel at the freezing level. At the bottom of the mixed layer (z = 0 km), the scaling parameter in Eqs. (7)-(8) is set to a value of zero. As z increases to 2 km, α is increased linearly to 1.0. Then above the 2 km, α has a constant value of 1.0. The parameter C takes into account the decrease in the fall speeds of graupel compared to water drops. A mean value of C equals to 2.5 for the mixed layer satisfies the requirement. Also, the value of scale height (H) for hydrometeors is 1.25

km in convective case, as mentioned earlier. The relationship of $m_{ow} = 0.1R$ is used to determine m_{ow} per volume [gm^{-3}] for a given rain rate [$mmhr^{-1}$]. The m_{ow} is assumed to be constant from the freezing level to the surface. Using the above procedure, the vertical profile of the hydrometeors in the convective region has been determined as a function of rain rate.

The particle size distributions in the convective column follow the gamma-type distribution, which has a form of

$$N(D) = N_o D^{\mu} \exp(-\lambda D) \tag{9}$$

where D is the diameter of the particle. The shape parameters of the distribution, N_o and μ are 1.9×10^7 m^{-4} and 1.0, respectively. The shape parameter is determined to match the graupel or the water hydrometeor content. This is based on convective particle size distribution properties.

In the theoretical simulation of the stratiform region, the cloud base is set near 4 km, and surface rain rate varies from 0.5 $mmhr^{-1}$ to 8.0 $mmhr^{-1}$. The profile of hydrometeors corresponding to stratiform rain used in the simulation is shown in Fig. 5b. The profile neglects the bright band and any evaporation below the freezing level. Above the freezing level, the vertical distribution of hydrometeors follows an exponential decay. The hydrometeors above the freezing level consist of mainly ice aggregates (snowflakes). The density of snowflakes is assumed to be 0.1 gcm^{-3}. Their fall speeds of the order of 1 ms^{-1} are parameterized as a function of altitude using the model of Locatelli and Hobbs (1974) and Foote and Du Toit (1969). As a result of these slow fall speeds, there is a relatively large accumulation of snow above the freezing level. In addition, since vertical velocity in stratiform region is weak, the depth of the mixed layer above the freezing level is assumed to be negligible. To conform to the shape of the PR reflectivity profile (Fig. 4), in this study the vertical profile of snow mass per unit volume of air above the freezing level is assumed to be decay exponentially with a scale height (H) of 1.0 km. The hydrometeor profile in stratiform region is given by the equation

$$m_s(z) = m_{os} \exp\left(-\frac{z}{H}\right) \tag{10}$$

where m_s and m_{os} are the snow mass per unit air volume and its value at the freezing level, respectively. The relationship of $m_{os} = 0.3R$ is used to determine m_{os} [gm^{-3}] for a give rain rate, R [$mmhr^{-1}$]. The m_{os} is assumed to be constant from the freezing level to the surface. Using the above procedure, the vertical profile of the hydrometeors in the stratiform region has been determined as a function of rain rate. The particle size distribution for the stratiform rain regime is represented by the gamma function mentioned earlier, except that N_o is $3.90\times10^7 m^{-4}$.

Taking the convective and stratiform hydrometeor vertical profiles described above, the height-dependent volume extinction coefficients for a given rain rate have been computed using the Mie calculation program of Wiscombe (1980). In the program, the calculated extinction efficiencies of spherical particles are weighted by the particle size distribution. The temperature-dependent real and imaginary parts of the refraction index for the rain drops needed in the program are adopted from the study of Ray (1972). For snow and graupel, a Maxwell-Garnett mixing formula (Meneghini and Liao, 2000) is assumed for deducing the real and imaginary refractive indices of air and ice mixtures.

The refractive index properties of particles that contain a mixture of air, ice, and water have not been considered in this study, because they are not definitive. The mixed-phase particles exist in the melting or 'bright band' layer in stratiform regions, and in the convective mixed-phase layer. Bauer *et al.* (2000) adopted the refractive index models of Meneghini and Liao (1996, 2000) to explain the emission properties of mixed-phase particles. Bauer *et al.* (2000) examined the refractive index properties of low-density, tenuous mixed-phase particles (snowflakes), and denser mixed-phase particles that have random distribution of air, ice and water. They also considered a mixture model that was non-uni-

Table 4. Simulation of T85 as a function of rain rate for convective rain models. Included on the table are the ice and water extinction optical depths above the freezing level. See text for explanation of convective/stratiform rain fraction and of adjusted rain rate in the convective model.

Rain rate ($mmhr^{-1}$)	Convective/Stratiform rain fraction (%)	Rain rate adjusted ($mmhr^{-1}$)	T85 (K)	Ice extinction optical depth	Water extinction optical depth
0.0	0.0/0.0	0.0	289.5	0.00	0.00
2.0	53.6/46.4	11.3	240.7	0.45	0.09
4.0	58.1/41.9	12.8	216.7	0.90	0.18
8.0	63.6/36.4	15.5	187.5	1.79	0.35
12.0	66.9/33.1	18.5	169.6	2.69	0.53
16.0	69.5/30.5	21.8	155.5	3.73	0.73
20.0	71.4/28.6	25.1	145.6	4.78	0.93
32.0	74.3/25.7	35.0	129.9	7.47	1.46

form, i.e., water-coated mixed-phase particles. They showed that the enhanced emission from the melting layer containing large tenuous snowflakes in the stratiform region could be as large as 30 K in the low frequency channels of the TMI, but it is significantly reduced to less than 10 K in the 85 GHz channel. Based on the above findings of the Bauer *et al.* study, it is assumed that including the detailed nature of mixed-phase particles is not critical for the purpose of radiative transfer modeling at 85 GHz in this study.

With the help of these extinction profiles, the upwelling brightness temperature at 85 GHz has been computed with a multiple-scattering radiative transfer model (previous Chapter), which assumes plane-parallel stratification with no horizontal inhomogeneities. The simulated T85 values are given in Table 4 for the convective regions, and in Table 5 for the stratiform regions. In the tables, the path integrated mass of water and ice, and their extinctions above the freezing level at each rain rate are also shown. Based on the path integrated water and ice extinctions in the stratiform region, it is inferred that when rain rate is greater than about 1 $mmhr^{-1}$, substantially less than 30% of the emission from the melting layer reaches the top of the atmosphere. This justifies the assumption that the emission from the melting layer can be neglected in this study.

Table 5. Simulation of T85 as a function of rain rate for stratiform rain models. Included on the table are the ice and water extinction optical depths above the freezing level. See text for explanation of convective/stratiform rain fraction.

Rain rate ($mmhr^{-1}$)	T85 (K)	Ice extinction optical depth	Water extinction optical depth
0.0	289.5	0.00	0.0
0.6	270.0	0.20	0.0
1.0	253.8	0.40	0.0
2.0	229.2	0.79	0.0
3.0	211.9	1.19	0.0
4.0	197.2	1.65	0.0
5.0	186.1	2.12	0.0
8.0	166.8	3.31	0.0
16.0	144.9	5.96	0.0

For the comparison with simulations, a plot of observed PR rain rate versus T85 given in Tables 2-3 is presented in Fig. 6. Note that these observations represent average of 20 km pixels in 20 K bins of T85. Here the convective rain rate clearly increases exponentially as T85 decreases, while the stratiform rain rate increases approximately in a linear pattern. In the same figure, similar plots of rain rate versus T85 deduced from simulations are presented (see Tables 4-5). It may be pointed out that the observed convective pixels have on average a percentage of convective rain that increases linearly from 56% to 73%, as T85 decreases from about 260 K to 120 K (see Table 2). In order to approximate this character, for a given value of T85 the simulated convective and stratiform rain rates have been combined taking into account their percentages given in Table 4. For this purpose, stratiform rain rates needed when T85 is less than 180 K have been estimated using the regression relationship between rain rate and simulated T85. No adjustments have been made in the stratiform

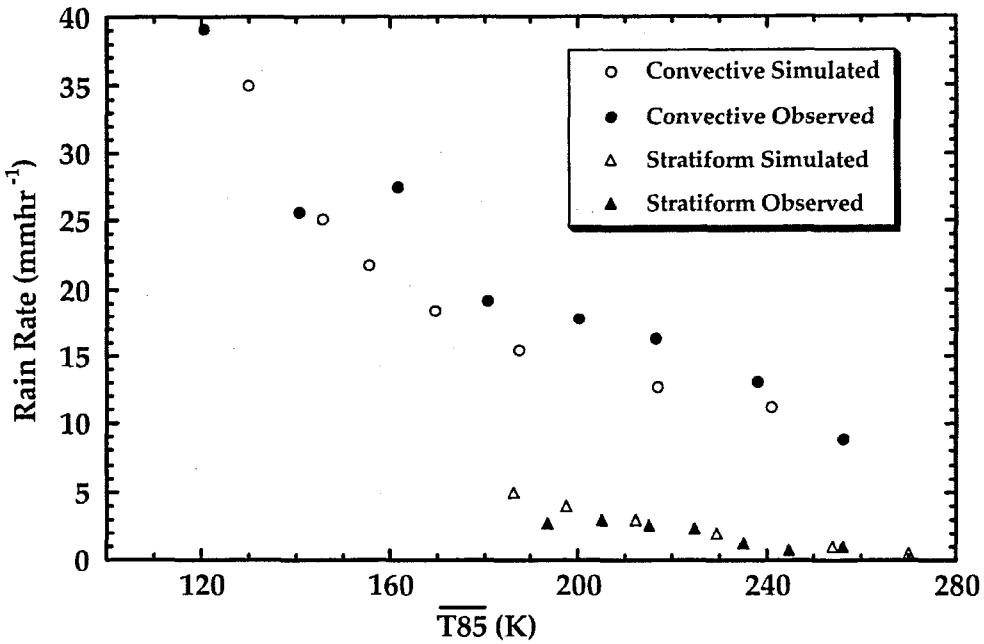

Fig. 6. Simulated and observed rain rate versus T85 relationships for convective and stratiform rain types. The plots symbols are defined in the panel inside the figure.

region. It has been hypothesized that when T85 of a convective pixel is around 260 K, the cloud is not deep enough to produce significant ice scattering in the 85 GHz channel, even though there is convective rain. For this reason, based on the observations in Fig. 1, the R is assumed to have a value close to 10 mmhr^{-1} to account for the fact that convective rain rate in pixels is generally greater than 10 mmhr^{-1} when T85 is below 260 K. Most likely this is warm rain, as pointed out by Petty (1999), who has suggested that passive microwave scattering-based estimates of precipitation miss warm rain events.

From Fig. 6, it is possible to explain from gross theoretical considerations the relationship between TMI T85 and PR rain rate given by the TRMM measurements. In the figure, the slope dR/dT85 given by linear regression for convective rain is three to four times larger than that for stratiform rain. This result is similar to that of Bennartz and Petty (2000).

In summary, to simulate the observations for convective rain, it is necessary to choose 1) the scale height of ice water content above the freezing level, 2) the mixed layer depth, and 3) the density of graupel. For stratiform rain, the variables to be prescribed are the scale height of the ice water content above the freezing level and the density of ice aggregates. Based on the above findings, it may be concluded that the large difference between convective and stratiform rain rate for a given value of T85 is due to the hydrometeor nature above the freezing level. Furthermore, much of the variability in the TRMM observations shown in Fig. 1 for the convective region may be due to that in the three parameters associated with convective rain.

DISCUSSION AND CONCLUSIONS

Physical processes that occur rain are highly variable in space and time. Understanding these processes with the help of observations and simulations is needed in deriving rainfall from microwave radiometer data. For this purpose, the information given by the PR and TMI onboard the TRMM satellite has been examined together with simulations for the

convective and stratiform rain regions in this study. In view of the fact that the radar and radiometer data are not collocated spatially, it is necessary to average these data to a scale of about 20 km. The average properties of the PR and TMI data presented in Tables 2-3 are very helpful to compare the observations from these two instruments. From these tables, one finds that the radiometer data in 19, 37, and 85 GHz channels are on the average redundant and have a poor ability to estimate convective and stratiform rain rates in an objective fashion. On the other hand, the PR reflectivities seem to have more robust information about these rain rates.

The TMI and PR observations over the tropical land show that there are two distinctly different relationships between T85 and PR rain rate in the convective and stratiform rain regions. As shown in Fig. 1, for a given change in rain rate, T85 varies much less in convective regions than in stratiform regions (see also Bennartz and Petty, 2001). It is possible to simulate these distinct relationships using separate models of radiative transfer for the convective and stratiform rain regions. The hydrometeor profile above the freezing level responsible for the weak extinction in convective regions is inferred to contain a substantial amount of supercooled water above the freezing level (see Table 4). On the other hand, strong extinction in the stratiform regions is inferred to result from an accumulation of slowly-falling low density ice aggregates (snow) above the freezing level. These theoretical results on the average explain the observations.

As in the case of the Z-R relationships of the PR, separate T85-R relationships can be derived for convective and stratiform rain regions. The discrimination of stratiform and convective rain is required for retrieving appropriate rain rate. Furthermore, like the Z-R relationships, the T85-R relationships need calibration with some ground truth. These calibrated relationships could then be applied to radiometer observations to retrieve rain rate. The usefulness of the high frequency T85 data has been emphasized in this study because of its small footprint size and strong extinction properties. This is evident from Figs. 3a-b, where T85 is plotted with respect to T37 and T19, respectively. It may be noted that the 85 GHz channel has significantly less surface contamination compared to other channels of the TMI, which means it is equally useful over land and ocean.

The high frequency channel at 85 GHz responds mainly to ice hydrometeors above the freezing level. On the other hand, the rain rate below the freezing level is often the required information. For this reason, one may consider high spatial resolution channels in the low frequency region, such as 6.6 and 10.7 GHz, to perform the remote sensing of rain. This is because these channels can give information about rain below the freezing level. However, these low frequency channels have weak extinction properties. This makes them poorly suited for retrieving rain rate over land, where surface emissivity is highly variable. Over ocean, the surface emissivity effects are relatively small, and can be minimized using two low frequency channels. For these reasons, the usefulness of lower frequency channels with high resolution may be limited to oceanic regions.

In the 3rd Algorithm Intercomparison Project (AIP-3), the data from surface radars were used to analyze the satellite microwave radiometer observations from TOGA-COARE (Ebert *et al.*, 1996). However, those radar and radiometer measurements were not simultaneous in time, and their spatial resolution was also significantly different. The information obtained from AIP-3 corresponding to the convective and stratiform rain is not as comprehensive as that given by TRMM. Understanding the relationship between the measurements made by microwave radiometers and convective and stratiform rain is necessary for the future Global Precipitation Measurement (GPM) mission. In the GPM a constellation of satellites with microwave radiometers are expected to be flown without accompanying radar. The current study has useful applications for rain-

fall retrieval and future satellite missions.

ACKNOWLEDGMENTS

This research is supported by the Climate Environment System Research Center sponsored by the SRC program of Korea Science and Engineering Foundation. The research is also performed during the sabbatical period of the author, provided by Ewha Womans University. The author would like to thank Si-Won Song at Seoul National University for arranging the manuscript.

REFERENCES

Balakrishnan, N. and Zrnic, D.S., 1990, Estimation of rain and hail rates in mixed-phase precipitation. Journal of the Atmospheric Sciences, 47, 565–583.

Bauer, P., Khain, A., Pokrovsky, A., Meneghini, R., Kummerow, C., Marzano, F., and Poiares Baptista, J.P.V., 2000, Combined cloud-microwave radiative transfer modeling of stratiform rainfall. Journal of the Atmospheric Sciences, 57, 1082–1104.

Bennartz, R. and Petty, G.W., 2001, The sensitivity of microwave remote sensing observations of precipitation to ice particle size distributions. Journal of Applied Meteorology, 40, 345–364.

Bringi, V.N., Knupp, K., Detwiler, A., Lui, L., Caylor, I.J., and Black, R.A., 1997, Evolution of a Florida thunderstorm during the Convective and Precipitation/ Electrification Experiment: The case of 9 August 1991. Monthly Weather Review, 125, 2131–2160.

Chandrasekhar, S., 1960, Radiative Transfer, Dover, Inc., New York, 393 p.

Ebert, E.E., Manton, M.J., Arkin, P.A., Allam, R.J., Holpin, G.E., and Gruber, A., 1996, Results from the GPCP algorithm Inter-comparison Programme. Bulletin of American Meteorological Society, 77, 2875–2887.

Foote, G.B. and Du Toit, P.S., 1969, Terminal velocity of raindrops aloft. Journal of Applied Meteorology, 8, 249–253.

Houze Jr., R.A., 1993, Cloud Dynamics. Academic Press, Inc., San Diego, 571 p.

Houze Jr., R.A., 1997, Stratiform precipitation in regions of convection: A meteorological paradox? Bulletin of American Meteorological Society, 78, 2179–2196.

Iguchi, T., Kozu, T., Meneghini, R., Awaka, J., and Okamoto, K., 2000, Rain-profiling algorithm for the TRMM Precipitation Radar. Journal of Applied Meteorology, 39, 2038–2052.

Liou, K., 1980, An Introduction to Atmospheric Radiation. Academic Press, Inc., Orlando, 392 p.

Locatelli, J.D. and Hobbs, P.V., 1974, Fall speeds and masses of solid precipitation particles. Journal of Geophysical Research, 79, 2185–2197.

Meneghini, R. and Liao, L., 1996, Comparisons of cross sections for melting hydrometeors as derived from dielectric mixing formulas and a numerical method. Journal of Applied Meteorology, 35, 1658–1670.

Meneghini, R. and Liao, L., 2000, Effective dielectric constants of mixed-phase hydrometeors. Journal of Atmospheric and Oceanic Technology, 17, 628–640.

Petty, G.W., 1999, Prevalence of precipitation from warm-topped clouds over Eastern Asia and the Western Pacific. Journal of Climate, 12, 220–229.

Ray, P.S., 1972, Broadband complex refractive indicies of ice and water. Applied Optics, 11, 1836–1843.

Sax, R.I. and Keller, V.W., 1980, Water-ice and water-updraft relationships near $-10^{\circ}C$ with populations of Florida cumuli. Journal of Applied Meteorology, 19, 505–514.

Sekhon, R.S. and Srivastava, R.C., 1970, Snow size spectra and radar reflectivity. Journal of the Atmospheric Sciences, 27, 299–307.

Short, D.A., Kucera, P.A., Ferrier, B.S., Gerlach, J.C., Rutledge, S.A., and Thiele, O.W., 1997, Shipboard radar rainfall patterns within the TOGA COARE IFA. Bulletin of American Meteorological Society, 78, 2817–2836.

Smith, P.L., Musil, D.J., Detwiler, A.G., and Ramachandran, R., 1999, Observations of mixed-phase precipitation within a CaPE thunderstorm. Journal of Applied Meteorology, 38, 145–155.

Wiscombe, W., 1980, Improved Mie scattering algorithms, Applied Optics, 19, 1505–1509.

Wu, R. and Weinman, J.A., 1984, Microwave radiances from precipitating clouds containing aspherical ice, combined phase, and liquid hydrometeors. Journal of Geophysical Research, 89, 7170–7178.

Zikmundu, J. and Vali, G., 1972, Fall patterns and fall velocities of rimed ice crystals. Journal of the Atmospheric Sciences, 29, 1334–1347.

Manuscript received October 22, 2001
Revised manuscript received November 14, 2001
Manuscript accepted November 26, 2001